

# Deterministic generation of parametrically driven dissipative Kerr soliton

MINGMING NIE,<sup>1,2</sup> AND SHU-WEI HUANG<sup>1</sup>

<sup>1</sup>Department of Electrical, Computer & Energy Engineering, University of Colorado Boulder, Boulder, CO 80309, USA

<sup>2</sup>email: Mingming.Nie@colorado.edu

\*Corresponding author: [ShuWei.Huang@colorado.edu](mailto:ShuWei.Huang@colorado.edu)

---

We theoretically study the nature of parametrically driven dissipative Kerr soliton (PD-DKS) in a doubly resonant degenerate micro-optical parametric oscillator (DR-D $\mu$ OPO) with the interplay of  $\chi^{(2)}$  and  $\chi^{(3)}$  nonlinearities. We show that there is a threshold group velocity mismatch above which single PD-DKS in DR-D $\mu$ OPO can be generated deterministically. We also find that the exact PD-DKS generation dynamics can be divided into two distinctive regimes depending on the phase matching condition. In both regimes, the perturbative effective third-order nonlinearity resulting from the cascaded quadratic process is responsible for the soliton annihilation and the deterministic single PD-DKS generation. We also develop the experimental design guidelines for accessing such deterministic single PD-DKS state. The principle of deterministic single PD-DKS alleviates the need for extensive dispersion engineering and thus it can be easily applied to different material platforms as a competitive ultrashort pulse and broadband frequency comb source architecture at the mid-infrared spectral range.

---

## 1. INTRODUCTION

Ultrafast optical parametric oscillator (OPO) has been demonstrated as a versatile and competitive optical frequency comb architecture [1-5] in otherwise difficult-to-access spectral ranges including the molecular fingerprinting mid-infrared region [6]. Recently, intriguing dissipative soliton dynamics in both synchronously pumped and continuous-wave (cw) pumped OPOs are observed and further utilized to enhance the performances of ultrafast OPOs [7-13]. In general, these ultrafast OPOs are restricted to the operation regime near the zero group velocity mismatch (GVM) point such that cascaded quadratic nonlinearity can be efficiently utilized for these quadratic frequency comb generation.

In addition, dissipative Kerr soliton (DKS) formation in fiber-feedback OPO has been observed by balancing the  $\chi^{(3)}$  nonlinearity and the group velocity dispersion (GVD) with a meter-long single mode fiber as well as the  $\chi^{(2)}$  parametric gain and the cavity loss with a millimeter-long periodically poled lithium niobate (PPLN) [14]. The unique example demonstrates how the combination of  $\chi^{(2)}$  and  $\chi^{(3)}$  nonlinearities in a singly resonant OPO can be utilized to facilitate signal DKS formation that enhances its stability and bandwidth. On the other hand, achieving such a clear separation between the  $\chi^{(2)}$  and  $\chi^{(3)}$  nonlinearities in chip-scale micro-OPOs ( $\mu$ OPOs) is very challenging if not impossible. In addition, most chip-scale  $\mu$ OPOs are doubly resonant and thus the effect of resonant pump must also be considered.

In this letter, we theoretically study the nature of signal DKS generation in a doubly resonant degenerate micro-OPO (DR-D $\mu$ OPO) with the interplay of  $\chi^{(2)}$  and  $\chi^{(3)}$  nonlinearities. In a recent experiment with an aluminum nitride (AlN) DR-D $\mu$ OPO, a unique deterministic single DKS generation dynamics has been demonstrated [15], but the

exact nature of the signal DKS remains obscure and the underlying physics has not been studied in details. Here we show for the first time that there is a threshold GVM above which single parametrically driven DKS (PD-DKS) in DR-D $\mu$ OPO can be generated deterministically. With the proper choice of GVM, material Kerr nonlinearity (MKN) will dominate the properties of PD-DKS while effective third-order nonlinearity from the competing cascaded quadratic process becomes soliton perturbation. The exact PD-DKS generation dynamics can be divided into two distinctive regimes depending on the phase matching condition. In both regimes, the perturbative effective third-order nonlinearity resulting from the cascaded quadratic process is responsible for the soliton annihilation and the deterministic single PD-DKS generation. Moreover, with large phase mismatch, deterministic single PD-DKS can be obtained with reduced GVM threshold but at the cost of higher pump power. Our theoretical analysis matches with the recent experimental observation [15] and provides the basis for detailed understanding of the phenomena. Finally, we have developed the experimental design guidelines for accessing such deterministic single PD-DKS state.

Of note, the deterministic single PD-DKS alleviates the need for extensive dispersion engineering and thus it represents an advantageous complement to the pure quadratic soliton mode-locking principle [8-13]. The concept of deterministic single PD-DKS can be easily applied to different material platforms, making it a competitive ultrashort pulse and broadband frequency comb source architecture at the mid-infrared spectral range.

## 2. THEORETIC ANALYSIS AND NUMERICAL RESULTS

The field evolution of a cw-pumped DR-DOPO with both  $\chi^{(2)}$  and  $\chi^{(3)}$  nonlinearities obeys the coupled equations in the retarded time frame:

$$\frac{\partial A}{\partial z} = \left[ -\frac{\alpha_{c1}}{2} - i\frac{k_1^*}{2} \frac{\partial^2}{\partial \tau^2} \right] A + i\kappa B A^* e^{-i\Delta k z} + i\left(\gamma_1 |A|^2 + 2\gamma_{12} |B|^2\right) A, \quad (1a)$$

$$\frac{\partial B}{\partial z} = \left[ -\frac{\alpha_{c2}}{2} - \Delta k' \frac{\partial}{\partial \tau} - i\frac{k_2^*}{2} \frac{\partial^2}{\partial \tau^2} \right] B + i\kappa A^2 e^{i\Delta k z} + i\left(\gamma_2 |B|^2 + 2\gamma_{21} |A|^2\right) B, \quad (1b)$$

and the boundary conditions:

$$A_{m+1}(0, \tau) = \sqrt{1 - \theta_1} A_m(L, \tau) e^{-i\delta_1}, \quad (2a)$$

$$B_{m+1}(0, \tau) = \sqrt{1 - \theta_2} B_m(L, \tau) e^{-i\delta_2} + \sqrt{\theta_2} B_{in}, \quad (2b)$$

where  $A$  is the signal field envelope,  $B$  is the pump field envelope,  $B_{in}$  is the cw pump,  $\alpha_{c1,2}$  are the propagation losses per unit length,  $\Delta k'$  is the GVM, and  $k_{1,2}^*$  are the GVD coefficients. Higher-order dispersion and nonlinearity are neglected for simplicity.  $\kappa = \sqrt{2}\omega_0 d_{eff} / \left( A_{eff} \sqrt{c^3 n_1^2 n_2 \epsilon_0} \right)$  is the normalized second-order nonlinearity coupling coefficient, where  $d_{eff}$  is the effective second-order nonlinear coefficient,  $A_{eff}$  is the effective mode area,  $c$  is the speed of light,  $\epsilon_0$  is the vacuum permittivity, and  $n_{1,2}$  are the refractive indices.  $\Delta k$  is the wave-vector mismatch,  $\gamma_{1,2}$  are self-phase modulation (SPM) coefficients and  $\gamma_{12}$  and  $\gamma_{21}$  are cross-phase modulation (XPM) coefficients.  $L$  is the nonlinear medium length,  $\theta_{1,2}$  are the coupler transmission coefficients and  $\delta_{1,2}$  are the pump-resonance and signal-resonance phase detuning, respectively.

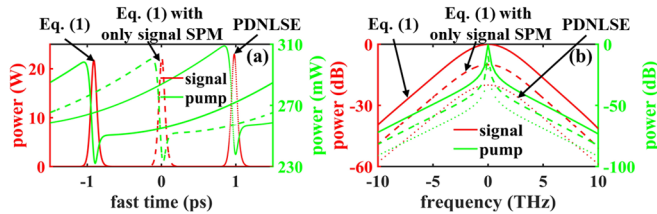


Fig. 1. Pulse profiles (a) and optical spectra (b) for signal field (red lines) and pump field (green lines), simulated with coupled-wave equations (solid), coupled-wave equations with only signal SPM (dashed), and PDNLSE (dotted). The pump of PDNLSE is calculated with Eq. (S8). The optical spectra are vertically shifted to emphasize the spectral shapes.

By solving the coupled-wave equations with detailed parameters (see Section S1, Supplement 1) via the standard split-step Fourier method, seeded generation of signal DKS pulse profile and optical spectrum are clearly shown in Fig. 1 (red solid lines). Due to the large GVM, the pump is only quasi-cw without any clear pulse profile (green solid lines in Fig. 1). Importantly, signal DKS can only exist when MKNs in Eq. (1) are included in the numerical simulation (see Section S2, Supplement 1), revealing the key role of MKN in the PD-DKS generation. We further find that the balance between signal SPM and signal GVD dominates the properties of PD-DKS (dashed lines in Fig. 1). It can be understood as the large GVM renders XPM ineffective and SPM by the weak quasi-cw pump is negligible. Our numerical simulation confirms that the PD-DKS is parametrically driven through the  $\chi^{(2)}$  OPO process while its anomalous GVD is balanced by the MKN  $\chi^{(3)}$  SPM process. The exact PD-DKS generation dynamics can be divided into two distinctive regimes depending on the phase matching condition.

### A. Deterministic single PD-DKS with perfect phase matching

With near perfect phase matching condition, Eq. (1)-(2) can be simplified into a single mean-field equation for the signal field, by only considering signal SPM effect (see Section S3, Supplement 1) under the mean-field and good cavity approximations:

$$t_r \frac{\partial A}{\partial t} = \left( -\alpha_1 - i\delta_1 - i\frac{k_1^* L}{2} \frac{\partial^2}{\partial \tau^2} \right) A + i\gamma_1 L |A|^2 A + i\mu A^* - \left[ \kappa L \text{sinc}(\xi) \right]^2 A^* \left[ A^2 \otimes J(\tau) \right], \quad (3)$$

where  $t$  is the “slow time” that describes the envelope evolution over successive round-trips,  $t_r$  is the signal roundtrip time,  $\tau$  is the “fast time” that depicts the temporal profiles in the retarded time frame,  $\alpha_{1,2}$  are the total linear cavity losses.  $\mu = \kappa L e^{i(\psi - \xi)} \text{sinc}(\xi) \sqrt{\theta_2} B_{in} / \sqrt{\delta_2^2 + \alpha_2^2}$ , is the phase-sensitive parametric pump driving term. Here  $\psi = -\arctan(\delta_2/\alpha_2)$  is the phase offset between the cw pump field  $B_{in}$  and the signal field  $A$ ,  $\xi = \Delta k L/2$  is the wave-vector mismatch parameter. Equation (3) is the parametrically driven nonlinear Schrödinger equation (PDNLSE) [8-10, 16] with a perturbation term representing cascaded quadratic process induced dispersive effective third-order nonlinearity  $J(\tau) = \mathcal{F}^{-1}[\hat{J}(\Omega)]$  where  $\hat{J}(\Omega) = (\alpha_2 + i\delta_2 - i\Delta k' L \Omega - i k_2^* L \Omega^2/2)^{-1}$  and  $\Omega$  is the offset angular frequency with respect to the signal resonance frequency. As shown in Fig. 1 with dotted lines, the validity of PDNLSE is verified and it provides a computationally efficient way to study the deterministic PD-DKS generation in this section.

Figures 2(a) and 2(b) shows the histogram of 100 independent intra-cavity average power traces with and without the perturbation term in Eq. (3), respectively. The pump phase detuning  $\delta_1$  is tuned linearly from blue to red side in 180 ns and held constant for another 70 ns to stabilize the PD-DKS generation. Each simulation starts with reinitialized noises to make sure there is no correlation between consecutive runs. Deterministic single PD-DKS formation is observed in Fig. 2(a), with each scan converging into the same intra-cavity power and single pulse shape (inset). We have to emphasize that this deterministic single PD-DKS generation is independent of the pump frequency scanning speed (see Section S4, Supplement 1). In contrast, Fig. 2(b) shows that the soliton number is random, exhibiting multiple solitons state or cw state. Therefore, it indicates the cascaded quadratic process induced perturbative effective third-order nonlinearity is the main reason for the deterministic single PD-DKS.

According to Eq. (3), the perturbation strength of the last term is proportional to the coefficient  $\left[ \kappa L \text{sinc}(\xi) \right]^2$  and  $J(\tau)$ . We will first study the effect of the latter with a given  $d_{eff}$  of 4 pm/V at perfect phase matching condition  $\xi=0$ . Similar to our previous study [8], we divide  $\hat{J}(\Omega) = X(\Omega) - iY(\Omega)$  into the real and imaginary parts to examine their effect independently, where  $X(\Omega)$  and  $Y(\Omega)$  resemble the dispersive two photon absorption (TPA) and the dispersive effective Kerr nonlinearity (EKN) respectively. Figures 2(c) and 2(d) plot the histogram of 100 overlaid intra-cavity average power traces during the frequency scanning process with only EKN and TPA effect, respectively. Deterministic single PD-DKS generation is observed in both simulations, indicating the contribution of both effects. On the other hand, EKN has a more profound effect on the PD-DKS peak power and pulse duration, due to its direct impact on the phase detuning, while TPA mainly increases the pump threshold because of the elevated loss. The influence of both effects on the pulse is also investigated with a test Gaussian pulse (see Section S5 in Supplement 1) and can be concluded as: (i) a sub-pulse appears right next to the main pulse; (ii) the intensity of the sub-pulse can be adjusted by GVM: smaller GVM results in larger sub-pulse intensity.

As shown in Figs. 3(a) and 3(b), with large GVM  $X(\Omega)$  and  $Y(\Omega)$  are both narrow-band with maximum values at the center frequency. Therefore, multiple solitons will experience long range interaction due to narrow-band perturbation. According to Eq. (3), this perturbation

from TPA or EKN effect can be viewed qualitatively as amplitude or phase modulation to the pump field ( $i\mu A^*$ ), which is a common method for deterministic DKS generation in  $\chi^{(3)}$  nonlinear cavities [17, 18]. Furthermore, the last term in Eq. (3) breaks down the phase symmetry  $A \rightarrow -A$ , which means solitons with opposite phase can no longer exist. Simulations show that single soliton with opposite phase will disappear with TPA effect or automatically adjust its phase and evolve into a soliton with EKN effect.

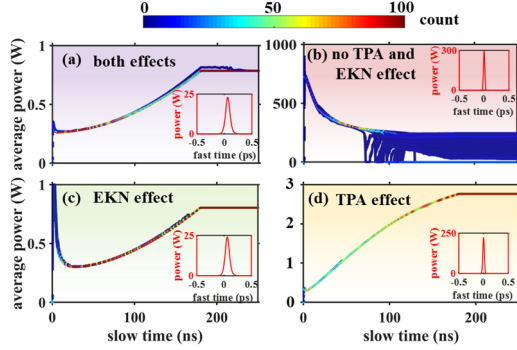


Fig. 2. Histogram of 100 overlaid intra-cavity average power traces via pump frequency scanning,  $|B_{in}|^2 = 30$  mW. (a) with both TPA and EKN effect; (b) without no TPA and EKN effect; (c) with only EKN effect; (d) with only TPA effect. The insets are the pulse profile of stable soliton. In the inset of (b), one of the multiple solitons is choose.

Figures 3(c) and 3(d) show how multiple solitons from Fig. 2(b) evolve under the influence of TPA and EKN, respectively. Similar to the avoided mode crossings induced Cherenkov radiation [19], TPA and EKN effect lead to dispersive waves and destabilize the solitons through long range interaction. Multiple solitons interact with each other, experience extra loss from the dispersive waves and finally only single soliton survives. Breathing behaviors are observed during the soliton interaction process, which is common due to the energy exchange between multiple solitons [19]. In addition, soliton interaction is more sensitive to EKN rather than TPA, similar to the more effective pump phase modulation method for conventional DKS generation. In fact, during the pump frequency scanning process in Fig. 2(c) and 2(d), single soliton usually arises from the highest intensity peak in the background [see Section S4, Supplement 1] instead of multiple solitons, resulting in no evident soliton steps for soliton annihilation.

Bandwidth of  $X(\Omega)$  and  $Y(\Omega)$  increases with the reduction of GVM, thus causing stronger soliton perturbation. With  $d_{eff} = 4$  pm/V, a GVM larger than 380 fs/mm is required to keep the soliton perturbation manageable so the PD-DKS can still sustain itself. With below-threshold GVM of 300 fs/mm, the PD-DKS breaks up into sub-pulses and eventually evolves into a cw solution [Fig. 3(e)]. Importantly, the GVM threshold increases as a function of  $d_{eff}$  [Fig. 3(f)] because larger  $d_{eff}$  means stronger soliton perturbation [Eq. (3)] and in turn requires larger GVM to alleviate the perturbative effect and stabilize the PD-DKS.

## B. Deterministic single PD-DKS with large phase mismatch

In the case of large phase mismatch, the single mean field equation Eq. (3) fails to describe the system dynamics since the coherent length is smaller than the cavity length. The integration along the cavity length from Eq. (1) to Eq. (S6) (see Section S3, Supplement 1) and the averaging effect of laser fields is invalid due to the strong energy exchange between pump and signal within one roundtrip. The comparative results of Eq. (1) and Eq. (3) in Fig. S5 (see Section S6, Supplement 1) indicate that PDNLSE is a good approximation only around the perfect phase matching point. Therefore, we will apply Eq. (1) along with the boundary conditions Eq. (2) to investigate deterministic PD-DKS generation with large phase mismatch in this section.

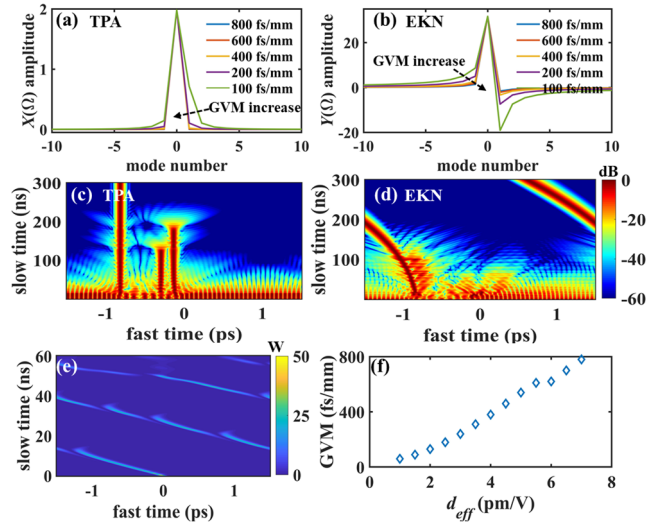


Fig. 3. The influence of TPA effect  $X(\Omega)$  (a) and EKN effect  $Y(\Omega)$  (b) on the cavity modes. Single soliton evolves from multiple solitons as a result of Fig. 2(b) under the TPA effect (c) and EKN effect (d). Both effects are increasing from zero to the maximum amplitudes. (e) pulse break-up due to large perturbation from effective third-order nonlinearity with a smaller GVM = 300 fs/mm. (f) GVM threshold versus second-order nonlinearity coefficient.

PD-DKS can also be achieved with large phase mismatch, at the cost of larger pump threshold. As shown in Figs. 4(a) and 4(b), the pump is no longer quasi-cw but becomes a Turing pattern with large modulation depth, corresponding to a strong spectral peak at  $\Delta\omega = 2\pi(\Delta kL)$ . Intuitively, Turing rolls is generated through GVM induced modulation instability where the modulation depth increases with  $\zeta$ . As for temporal dynamics, Figs. 4(c) and 4(d) show the evolution of signal and pump field within three successive roundtrips. In the retarded time frame of the signal, the pump Turing roll drifts at a speed of  $1/\Delta k$  in the cavity but remains locked to the PD-DKS after each roundtrip, resulting from the temporal separation of  $\Delta kL$  between adjacent Turing rolls. This can be understood by regarding Turing rolls as potential wells where the PD-DKS just hops across one during each roundtrip. The pulse duration of PD-DKS gets shorter with higher peak power when GVM decreases as Turing rolls become narrower. In addition, the intracavity pump experiences a small temporal shift [see the inset of Fig. 4(d)] at the coupler region when it meets with the external cw drive.

Figure 4(e) shows the histogram of 100 overlaid intra-cavity average power traces with pump frequency tuning. Deterministic single PD-DKS formation is observed in simulations. The determinism still comes from the perturbative effective third-order nonlinearity, which can be understood qualitatively with Eq. (3) although it can not exactly describe the system dynamics. Of note, large phase mismatch reduces the magnitude of effective third-order nonlinearity and in turn lowers the threshold GVM to keep the effective third-order nonlinearity perturbative in comparison to the MKN. Comparing Fig. 4(f) with Fig. 3(f), it is shown the threshold GVM above which single PD-DKS can be deterministically generated is lowered by almost an order of magnitude when a wave-vector mismatch parameter  $\zeta$  of  $0.75\pi$  is introduced.

## C. Discussion

Based on the previous analysis, moderate perturbation induced by cascaded quadratic process is necessary to achieve the deterministic single PD-DKS. The interplay between  $d_{eff}$ , GVM, and  $\zeta$  uniquely define the evolution dynamics. Strong perturbation from effective third-order nonlinearity can be alleviated by lowering the strength of cascaded quadratic process through the reduction of  $d_{eff}$ , the increase of  $\zeta$ , or the enhancement of GVM.



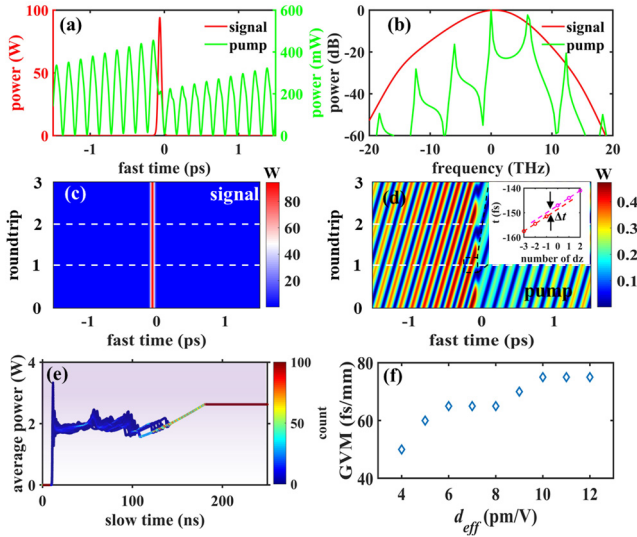


Fig. 4. Signal soliton with large phase mismatch.  $\zeta=0.75\pi$ ,  $|B_{nl}|^2=100$  mW. (a) pulse profiles and (b) spectra. Pulse evolution within three successive roundtrips (indicated by white dashed lines) for signal (c) and pump field (d). The inset of (d) shows the temporal positions in time axis corresponding to peak powers before and after meeting with pump. (e) Histogram of 100 overlaid intra-cavity average power traces with same frequency scanning strategy in Fig. 2. (f) GVM threshold versus second-order nonlinearity coefficient.

To experimentally access the deterministic single PD-DKS state, one has to consider how these three parameters co-determine the system's behavior as well as the experimental restrictions: (i) GVM can be tuned via dispersion engineering [20] but it ultimately limited by material dispersion; (ii)  $d_{eff}$  can be changed by choosing different nonlinear crystals or different crystal axes; (iii)  $\zeta$  is the most controllable parameter in experiment, through temperature tuning, angle tuning, quasi-phase-matching, and more. Admitting the above-mentioned experimental restrictions, the design rules to experimentally access deterministic PD-DKS can be summarized as: (i) for small  $d_{eff}$ , it is better to operate near the perfect phase matching point to lower the pump threshold; however, the GVM threshold is higher in this regime; (ii) for large  $d_{eff}$ , it is better to operate with large phase mismatch to lower the GVM threshold; compromise between the GVM threshold and pump threshold should be considered in this regime.

According to the experimental guidelines, the deterministic single PD-DKS in the AlN DR-D $\mu$ OPO [15] is believed to be the consequence of relatively large MKN, large GVM, and relatively small  $d_{eff}$ . The simulated results (see Section S7, Supplement 1) including the soliton spectrum and corresponding dynamics, agree excellently with the experimental ones in Ref. [15]. What's more, we numerically obtain the GVM induced small pump spectral peaks, which is clearly shown in the experiment but is not well explained.

### 3. CONCLUSION

In conclusion, we theoretically study the nature of PD-DKS generation in a DR-D $\mu$ OPO with the interplay of  $\chi^{(2)}$  and  $\chi^{(3)}$  nonlinearities. With the proper choice of GVM, MKN will dominate the properties of PD-DKS while effective third-order nonlinearity from the competing cascaded quadratic process becomes soliton perturbation. The exact PD-DKS generation dynamics can be divided into two distinctive regimes depending on the phase matching condition. In both regimes, the perturbative effective third-order nonlinearity resulting from the cascaded quadratic process is responsible for the soliton annihilation and the deterministic single PD-DKS generation. Moreover, with large phase mismatch, deterministic single PD-DKS can be obtained with reduced GVM threshold but at the cost of higher pump power. To access the deterministic single PD-DKS state, it is thus better to operate near

the perfect phase matching point with low  $d_{eff}$  materials while it is beneficial to operate at large phase mismatch when high  $d_{eff}$  materials are available.

Importantly, the deterministic single PD-DKS alleviates the need for extensive dispersion engineering and thus the working principle can be easily applied to different material platforms, making it a competitive ultrashort pulse and broadband frequency comb source architecture at the mid-infrared spectral range.

**Funding.** Office of Naval Research (N00014-19-1-2251).

**Disclosures.** The authors declare no conflicts of interest.

See Supplement 1 for supporting content.

### REFERENCES

1. A. Esteban-Martin, G. K. Samanta, K. Devi, S. Chaitanya Kumar, and M. Ebrahim-Zadeh, *Opt. Lett.* **37**, 115 (2012).
2. K. Devi, S. C. Kumar, and M. Ebrahim-Zadeh, *Opt. Lett.* **37**, 3909 (2012).
3. V. Ulvila, C. R. Phillips, L. Halonen, and M. Vainio, *Opt. Lett.* **38**, 4281 (2013).
4. V. Ulvila, C. R. Phillips, L. Halonen, and M. Vainio, *Opt. Express* **22**, 10535 (2014).
5. S. Mosca, M. Parisi, I. Ricciardi, F. Leo, T. Hansson, M. Erkintalo, P. Maddaloni, P. De Natale, S. Wabnitz, and M. De Rosa, *Phys. Rev. Lett.* **121**, 093903 (2018).
6. A. Schliesser, N. Picqué, and T. W. Hänsch, *Nat. Photon.* **6**, 440 (2012).
7. M. Jankowski, A. Marandi, C. R. Phillips, R. Hamerly, K. A. Ingold, R. L. Byer, and M. M. Fejer, *Phys. Rev. Lett.* **120**, 053904 (2018).
8. M. Nie, and S.-W. Huang, *Opt. Lett.* **45**, 2311 (2020).
9. M. Nie, and S.-W. Huang, *Opt. Lett.* **45**, 4184 (2020).
10. M. Nie, and S.-W. Huang, *Phys. Rev. Appl.* **13**, 044046 (2020).
11. P. Parra-Rivas, L. Gelens, and F. Leo, *Phys. Rev. E* **100**, 032219 (2019).
12. P. Parra-Rivas, C. Mas-Arabi, and F. Leo, *Phys. Rev. A* **101**, 06381 (2020).
13. A. Sheng, C. Xi, Z. Yang, X. Jiang, G. He, *IEEE Photon. J.* **12**, 6100607 (2020).
14. C. F. O'Donnell, S. C. Kumar, T. Paoletta, and M. Ebrahim-Zadeh, *Optica* **7**, 426 (2020).
15. A. W. Bruch, X. Liu, Z. Gong, J. B. Surya, M. Li, C.-L. Zou, and H. X. Tang, *Arxiv*, <https://arxiv.org/pdf/2004.07708.pdf>
16. I. V. Barashenkov, and E. V. Zemlyanaya, *Phys. Rev. Lett.* **83**, 2568 (1999).
17. Y. Wang, B. Garbin, F. Leo, S. Coen, M. Erkintalo, and Stuart G. Murdoch, *Opt. Lett.* **43**, 3192 (2018).
18. D. C. Cole, J. R. Stone, M. Erkintalo, K. Y. Yang, X. Yi, K. J. Vahala, and S. B. Papp, *Optica* **5**, 1304 (2018).
19. C. Bao, Y. Xuan, D. E. Leaird, S. Wabnitz, M. Qi, A. M. Weiner, *Optica* **4**, 1011 (2017).
20. Y. Guo, Z. Jafari, L. Xu, C. Bao, P. Liao, G. Li, A. M. Agarwal, L. C. Kimerling, J. Michel, A. E. Willner, and L. Zhang, *Photonics Res.* **7**, 1279 (2019).

## REFERENCES

1. A. Esteban-Martin, G. K. Samanta, K. Devi, S. Chaitanya Kumar, and M. Ebrahim-Zadeh, "Frequency-modulation-mode-locked optical parametric oscillator," *Opt. Lett.* **37**, 115 (2012).
2. K. Devi, S. C. Kumar, and M. Ebrahim-Zadeh, "Mode-locked, continuous-wave, singly resonant optical parametric oscillator," *Opt. Lett.* **37**, 3909 (2012).
3. V. Ulvila, C. R. Phillips, L. Halonen, and M. Vainio, "Frequency comb generation by a continuous-wave-pumped optical parametric oscillator based on cascading quadratic nonlinearities," *Opt. Lett.* **38**, 4281 (2013).
4. V. Ulvila, C. R. Phillips, L. Halonen, and M. Vainio, "High-power mid-infrared frequency comb from a continuous-wave-pumped bulk optical parametric oscillator," *Opt. Express* **22**, 10535 (2014).
5. S. Mosca, M. Parisi, I. Ricciardi, F. Leo, T. Hansson, M. Erkintalo, P. Maddaloni, P. De Natale, S. Wabnitz, and M. De Rosa, "Modulation instability induced frequency comb generation in a continuously pumped optical parametric oscillator," *Phys. Rev. Lett.* **121**, 093903 (2018).
6. A. Schliesser, N. Picqué, and T. W. Hänsch, "Mid-infrared frequency combs," *Nat. Photon.* **6**, 440 (2012).
7. M. Jankowski, A. Marandi, C. R. Phillips, R. Hamerly, K. A. Ingold, R. L. Byer, and M. M. Fejer, "Temporal Solitons in Optical Parametric Oscillators," *Phys. Rev. Lett.* **120**, 053904 (2018).
8. M. Nie, and S.-W. Huang, "Quadratic soliton mode-locked degenerate optical parametric oscillator," *Opt. Lett.* **45**, 2311 (2020).
9. M. Nie, and S.-W. Huang, "Symbiotic quadratic solitons mode-locked non-degenerate optical parametric oscillators," *Opt. Lett.* **45**, 4184 (2020).
10. M. Nie, and S.-W. Huang, "Quadratic Solitons in Singly Resonant Degenerate Optical Parametric Oscillators," *Phys. Rev. Appl.* **13**, 044046 (2020).
11. P. Parra-Rivas, L. Gelens, and F. Leo, "Localized structures in dispersive and doubly resonant optical parametric oscillators," *Phys. Rev. E* **100**, 032219 (2019).
12. P. Parra-Rivas, C. Mas-Arabí, and F. Leo, "Parametric localized patterns and breathers in dispersive quadratic cavities," *Phys. Rev. A* **101**, 06381 (2020).
13. A. Sheng, C. Xi, Z. Yang, X. Jiang, G. He, "Quadratic Soliton Combs in Doubly Resonant Dispersive Optical Parametric Oscillators," *IEEE Photon. J.* **12**, 6100607 (2020).
14. C. F. O'Donnell, S. C. Kumar, T. Paoletta, and M. Ebrahim-Zadeh, "Widely tunable femtosecond soliton generation in a fiber-feedback optical parametric oscillator," *Optica* **7**, 426 (2020).
15. A. W. Bruch, X. Liu, Z. Gong, J. B. Surya, M. Li, C.-L. Zou, and H. X. Tang, "Pockels Soliton Microcomb," *Arxiv*, <https://arxiv.org/pdf/2004.07708.pdf>
16. I. V. Barashenkov, and E. V. Zemlyanaya, "Stable complexes of parametrically driven, damped nonlinear Schrödinger solitons," *Phys. Rev. Lett.* **83**, 2568 (1999).
17. Y. Wang, B. Garbin, F. Leo, S. Coen, M. Erkintalo, and Stuart G. Murdoch, "Addressing temporal Kerr cavity solitons with a single pulse of intensity modulation," *Opt. Lett.* **43**, 3192 (2018).
18. D. C. Cole, J. R. Stone, M. Erkintalo, K. Y. Yang, X. Yi, K. J. Vahala, and S. B. Papp, "Kerr-microresonator solitons from a chirped background," *Optica* **5**, 1304 (2018).
19. C. Bao, Y. Xuan, D. E. Leaird, S. Wabnitz, M. Qi, A. M. Weiner, "Spatial mode-interaction induced single soliton generation in microresonators," *Optica* **4**, 1011 (2017).
20. Y. Guo, Z. Jafari, L. Xu, C. Bao, P. Liao, G. Li, A. M. Agarwal, L. C. Kimerling, J. Michel, A. E. Willner, and L. Zhang, "Ultra-flat dispersion in an integrated waveguide with five and six zero-dispersion wavelengths for mid-infrared photonics," *Photonics Res.* **7**, 1279 (2019).